land

Article

Spatial and Temporal Characteristics of Evapotranspiration in the Upper Minjiang River Basin Based on the SiB2 Model

Bo Kong [1], Bing He [2,*], Xiangmeng Liu [3] and Huan Yu [3]

1 Institute of Mountain Hazards and Environment, Chinese Academy of Sciences, Chengdu 610299, China; kongbo827@imde.ac.cn
2 School of Computer Science, Chengdu University of Information Technology, Chengdu 610225, China
3 College of Geosciences, Chengdu University of Technology, Chengdu 610059, China; xiangmeng_liu@126.com (X.L.); yuhuan0622@126.com (H.Y.)
* Correspondence: bingh@cuit.edu.cn

Abstract: The evapotranspiration (ET) in mountainous watersheds affects the security of downstream water supply and ecological safety. Continuous time-varying ET cannot be obtained by traditional methods such as remote sensing and ground observations. In this study, a simple biosphere model 2 (SiB2) was parameterized in a typical mountainous area, the upper Minjiang River, using field observations and remote sensing data. The performance of SiB2 was then assessed by comparing it with direct measurements of the evaporation dishes. The results showed that (1) at the daily scale, the simulated ET was smaller than the measured ET. At the monthly scale, the relative errors between the simulated and measured values ranged from 1.48% to 20.72%. The relative error between the simulated and measured values of the total annual ET is 6.99%; (2) the ET of Minjiang River was characterized by a "bimodal" variation, with lower daily ET from November to February (non-growing season) and higher daily ET from March to August (growing season); (3) the ET of Minjiang River showed the spatial characteristics of low in the northwest and high in the southeast, with a high-value center located in Dujiangyan City. In summary, SiB2 is suitable for simulating ET in mountainous watersheds with spatial and temporal continuity. This study can contribute to the enhancement of water resources use planning and basin management in the upper Minjiang River.

Keywords: remote sensing; hydrothermal flux; watershed hydrology; land surface process

Citation: Kong, B.; He, B.; Liu, X.; Yu, H. Spatial and Temporal Characteristics of Evapotranspiration in the Upper Minjiang River Basin Based on the SiB2 Model. *Land* **2022**, *11*, 1141. https://doi.org/10.3390/land11081141

Academic Editor: Sanghyun Lee

Received: 2 June 2022
Accepted: 18 July 2022
Published: 25 July 2022

1. Introduction

Mountainous areas account for about 24% of the global land area and 2/3 of the land area of China. They provide an important ecological function in regulating regional and global climate, maintaining ecosystem biodiversity, and conserving water [1]. Currently, global climate change and overuse of water resources by humans have led to water scarcity and derived ecological and environmental problems, which greatly affect the healthy development of human-land systems in mountainous areas. Evapotranspiration (ET) is one of the key aspects of surface water and heat balance [2] and an essential component of the hydrological cycle in watersheds. However, there are challenges in installing and maintaining meteorological instruments in mountainous areas at high altitudes, and the spatial resolution of the obtained meteorological data is low [3]. Therefore, an analysis of the spatial and temporal characteristics of ET in mountainous watersheds based on a long-term time series will be beneficial for water resources management and weather forecasting in ecologically fragile mountainous watersheds [4–7].

The ET models for describing water consumption patterns have served as one of the decision support tools for agricultural and forestry development. Over the years, the ET models have evolved from single-point observations to methods with biophysical significance. Most of the traditional methods for estimating ET are based on single-point calculations from ground-based observation equipment, such as Bowen Ratio [8], Eddy

Covariance [9] and large aperture scintillometer [10]. Although ground-based observations allow more accurate acquisition of ET at single locations, field and smaller landscape scales, it is difficult to directly extrapolate these observations to large spatial scales due to land surface heterogeneity, especially for watersheds with LULC (land use/land cover) variability [11]. Remote sensing technology is able to provide visible, near infrared and thermal infrared wavelengths to extract parameters related to surface evapotranspiration and energy transfer processes and has obvious advantages in monitoring regional ET under non-uniform ground surfaces. Remote sensing-based methods can be divided into two categories: surface energy balance (SEB) models and meteorological-based models. The commonly used SEB models are SEBAL [12], SEBS [13], METRIC [14,15], S-SEBI [16], and TESEBS [17]. Among them, SEBAL and SEBS are two representative models that estimate the sensible heat fluxes based on the observed data and calculate the latent heat fluxes based on the SEB equation [12,13]. Meteorological-based models are usually based on physical methods such as the Penman–Monteith (P-M) [18] and the Priestley–Taylor [6]. Remote sensing technology allows rapid access to real-time, large-scale data [19,20], and has facilitated the estimation and analysis of ET. However, the meteorological data, model structures, and parameterization methods used lead to significant differences in the accuracy and applicability of each product. This difference is exacerbated by the complexity of the mountainous terrain. Factors such as altitude, slope direction and gradient directly affect the radiation income and expenditure and surface temperature distribution in the mountain environment, which in turn affect the land surface parameters required for evapotranspiration inversion, such as surface albedo, and this inevitably brings some bias to the results of remote sensing-based evapotranspiration estimation [14].

The remote sensing-based models can only calculate the land surface ET at the moment of satellite transit and cannot produce the time-continuous ET. In this context, the Land Surface Process Model (LSPM) has been widely used in a long series of regional ET simulation to studies on the material and energy exchange between the land-atmosphere. LSPM has evolved from a simple "bucket" model to a highly physical SVAT (soil–vegetation–atmosphere transport scheme) [21]. Currently, typical SVAT models include BATS [22], SiB (Simple Biosphere Model) [23], SiB2 [24], VIC (Variable Infiltration Capacity) [25], and CoLM (Common Land Model) [26]. SiB2 is one of the most representative LSPM. It can be used to calculate the energy, material, and momentum transport between the atmosphere and vegetation surface to realize the coupling of photosynthesis and water vapor transport. It is widely used to simulate the energy and water exchange between the land surface and the atmosphere [27,28]. It has also been applied to watershed land surface energy and water balance research [29]. The SiB2 requires many input parameters related to soil and vegetation properties, which limits its application on a regional scale. To the best of the author's knowledge, evapotranspiration studies in high-altitude watersheds are limited, and SiB2 has only been applied to simulate evapotranspiration from some watersheds [30] and agricultural lands [31]. Therefore, this approach needs more validation in mountainous areas.

Basin water resources management, hydrological processes and climate change impact studies need to be supported by large-scale, continuous dynamic ET data. The upper Minjiang River is a typical ecologically fragile area in southwest China and an important ecological barrier in the upper reaches of the Yangtze River. Previous studies have investigated ET in this region based on different modeling approaches. Zhang [32] used a modified Thornthwaite model [33] to calculate potential evapotranspiration (PET) for four watersheds from 1992 to 1998. Other studies used the Fu Baopu model [34–36] based on the complementary correlation theory, but few studies have explored intra-annual evapotranspiration. Given the labor- and cost-intensive nature of in situ ET measurements and the transient shortcomings of remote sensing inversion, LSPM is considered a promising alternative method for estimating ET in this region. The continuous ET characteristics of the upper Minjiang River are less explored, and the applicability of LSPM in this region needs further investigation. In this context, the main objective of our study was to assess the ability of SiB2 to simulate ET in the upper Minjiang River and the spatial and temporal characteristics of ET in this region.

In this study, field measurements and model simulations of ET are integrated and analyzed. (1) The continuous ET is estimated based on SiB2 using the meteorological forcing data of China to investigate the intra-annual dynamic characteristics of the watershed ET; (2) The applicability of SiB2 under mountainous areas is verified using daily-scale ET observations from the meteorological station in Lixian and the simulated ET results; (3) The relationship and differences between ET and temperature, precipitation and elevation in the upper Minjiang River are investigated. This study has two main contributions. First, unlike previous studies on ET based on remote sensing, this paper validated the applicability of SiB2 in complex mountainous areas in terms of temporal continuity. Second, compared with the existing studies on ET in the upper Minjiang River, this paper analyzed the spatial and temporal characteristics of intra-annual ET and its relationship with meteorological and environmental factors.

2. Study Area

Minjiang River is the largest tributary of the upper reaches of the Yangtze River. The upper Minjiang River is located in the northwestern part of the Sichuan Basin and the eastern part of the Qinghai-Tibet Plateau (Figure 1). It includes the five counties of Wenchuan (WC), Lixian (LX), Maoxian (MX), Heishui (HS), Songpan (SP) and Dujiangyan (DJY). The mountainous area of this region is over 40%, and the average slope is over 30°. The entire area has a large topographic elevation difference (ranging from 764 m to 6250 m), sloping from northwest to southeast. There are many water systems in the area, mostly developing plume water systems. It has a high vegetation cover and is the "green barrier" of the Chengdu Plain. In the classification of fragile ecosystem types in China, it is classified as a fragile ecosystem in the southern mountainous areas. Its climate is characterized by a highland monsoon, in which the mountain temperate and mountain subtropical climates predominate. It is strongly influenced by the high westerly circulation as well as the southwest and southeast monsoons, resulting in distinct wet and dry seasonal characteristics. The recharge of water sources is dominated by rainfall [37]. The average annual temperature in this basin ranges from 5 °C to 15 °C.

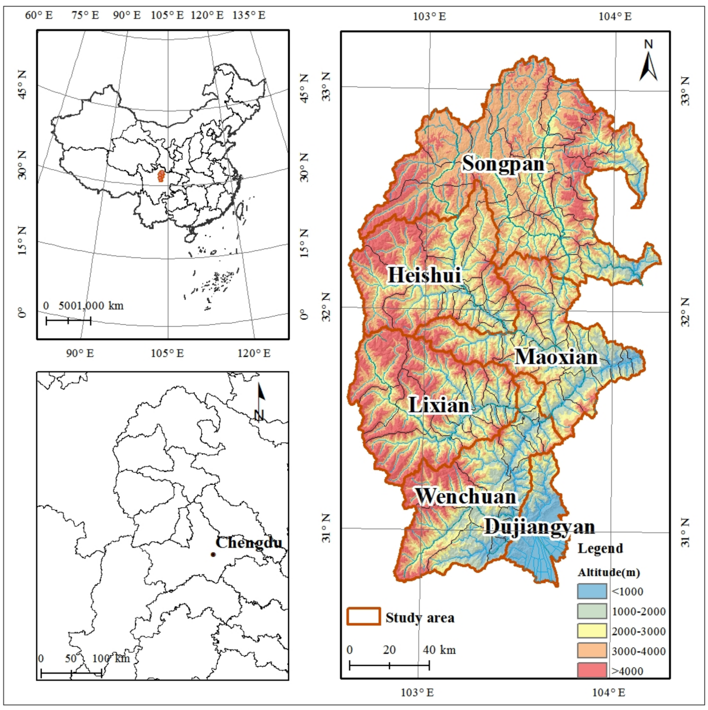

Figure 1. Study area.

3. Data and Methods

3.1. Dataset

The data used in the study include: CMFD (China Meteorological Forcing Dataset), DEM, LULC (Land use/Land cover), soil type, NDVI and daily evapotranspiration from meteorological stations.

CMFD was downloaded from the National Tibetan Plateau/Third Pole Environment Data Center [38] and was mainly used to provide six forcing variables such as downgradient shortwave radiation, downgradient longwave radiation, air temperature, water vapor pressure, horizontal wind speed at anemometer height, and precipitation for the SiB2 simulation. The CMFD dataset uses Princeton reanalysis data, GEWEX-SRB (Global Energy and Water Exchanges-Surface Radiation Budget), GLDAS (Global Land Data Assimilation System) and TRMM (Tropical Rainfall Measuring Mission) as background fields and integrates meteorological observations from the CMA (China Meteorological Administration). The CMFD covers the period 1979–2015 with a temporal resolution of 3 h and a spatial resolution of 0.1°.

SRTM (Shuttle Radar Topography Mission) were downloaded from the RESDC (Resource and Environmental Science Data Center of the Chinese Academy of Sciences) [39] and used to extract the average slope required for SiB2. LULC maps for 2010 were downloaded from the NCDC (national cryosphere desert data center) [40] and used to extract the nine vegetation types needed in the SiB2 model. The Chinese soil data set at 1:1 million were downloaded from the NCDC [40] and used to establish the required soil type parameters in the SiB2 model. Soil texture data were downloaded from the RESDC [39]. Monthly vegetation index (NDVI) data from December 2012 to December 2013 were downloaded from the RESDC [39] and used to calculate vegetation parameters with time dynamics. The available links for the above data are shown in Appendix A Table A1.

3.2. Methods

In this study, remote sensing, meteorological, land use/land cover, soil and DEM data were first processed using GIS technology. This step is the basis of the SiB2 simulation process. The SiB2 model was then run hourly with prepared input parameters to obtain output variables. Both of these steps serve the subsequent analysis step, which is the most important part of this study. The data preparation process and the key components of the ET simulation in SiB2 are described below (as shown in Figure 2).

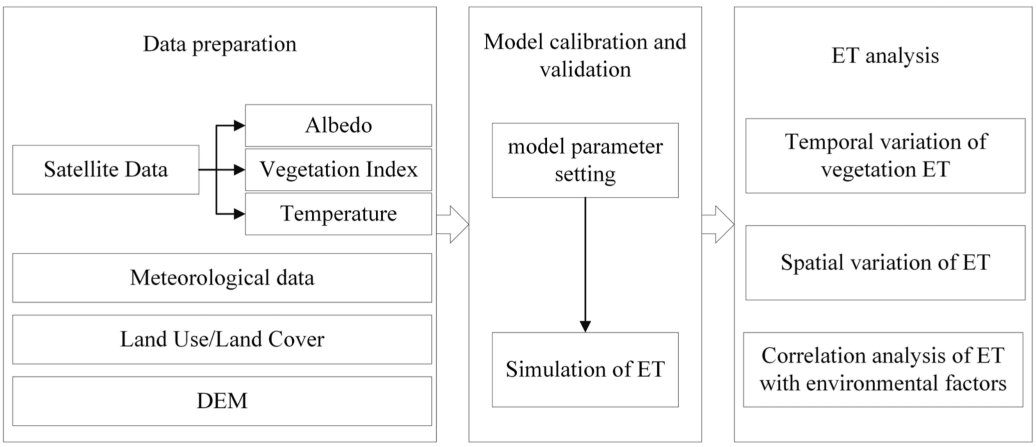

Figure 2. Flow chart of the research methodology.

3.2.1. Data Preparation and Parameter Setting

Numerical simulations using the SiB2 model require a parametric approach. SiB2 includes six forcing variables: downward longwave radiation, downward shortwave radiation, air temperature, precipitation, water vapor pressure, and wind speed at the anemometer height.

First, to facilitate the reading and writing of the SiB2 program, each pixel value in the CMFD data was converted to ASCII format and the driving data such as downgradient shortwave radiation, downgradient longwave radiation, air temperature, water vapor pressure, horizontal wind speed, and precipitation at the measured height were extracted for the study period. The water vapor pressure was obtained by converting the air pressure and specific humidity variables in CMFD.

$$v = qP/(0.622 + 0.378q) \tag{1}$$

where v is water vapor pressure (Pa), q is near-surface air specific humidity (Kg/Kg), and P is surface air pressure (Pa).

Second, the terrain slope in the study area was obtained using the DEM data, and the gridded data of the study area was created according to the resolution $0.1^\circ \times 0.1^\circ$ as well as the average slope within each grid was extracted using the zoning statistical analysis tool in ArcGIS 10.1.

Third, based on the collected LULC data, the LULC types were aggregated according to the nine vegetation types defined by the SiB2 model, and the final vegetation types in the study area were determined as 1 (Evergreen Broadleaf Forest, EBF), 2 (Deciduous Broadleaf Forest, DBF), 4 (Evergreen Coniferous Forest, ECF), 6 (Short Vegetation/C4 Grassland, SVCG), 7 (Broadleaf Shrubs on Bare Soil, BSBS), and 9 (Agricultural Land/C3 Grassland, ALCG) (shown in Appendix A Table A2), in addition to morphological parameters, optical property parameters, and physiological parameters of vegetation (as shown in Appendix A Tables A3–A6). Considering the uneven LULC in each region after gridding, the area proportion of each vegetation type in each grid was calculated by using the zoning statistics tool in ArcGIS, and the vegetation type with largest area was selected as the vegetation type as the grid value for simulation.

Fourth, since the soil data had some missing values which were gap-filled with reference to the soil texture data, the soil data were simplified according to the seven soil types defined by SiB2, and the soil texture types in the study area were finally determined to include 1 (Sandy), 2 (Sandy Loam), 3 (Loam), 4 (Clay Loam-Sandy Clay Loam), and 5 (Clay-Clay Loam). The soil texture type with the largest area in each grid was selected using the zoning statistics tool in ArcGIS. Finally, the average NDVI values within each grid were extracted using the zoning statistical tool.

3.2.2. Model Simulation

SiB2 is mainly used to simulate the energy (including net radiation, sensible and latent heat fluxes), evapotranspiration, and CO_2 exchange between the land surface and the atmosphere. In the SiB2 structure, the vegetation types in the SiB model are integrated, while the two vegetation canopy layers are simplified into a one-layer structure. There are eight control equations and several diagnostic equations in the SiB2, which are described in Sellers' paper [23,24]. The control equations mainly control the energy and water balance between the canopy and the land surface and the soil and determine the energy and water exchange between them and the atmosphere. The diagnostic equations are used to calculate the energy, water and momentum exchange between vegetation and atmosphere, soil and vegetation, and the soil-atmosphere interface. The land surface flux simulation of SiB2 is borrowed similar to Ohm's law to describe the energy and water exchange between vegetation, soil and the surrounding air. The simulation process of SiB2 is shown in Figure 3.

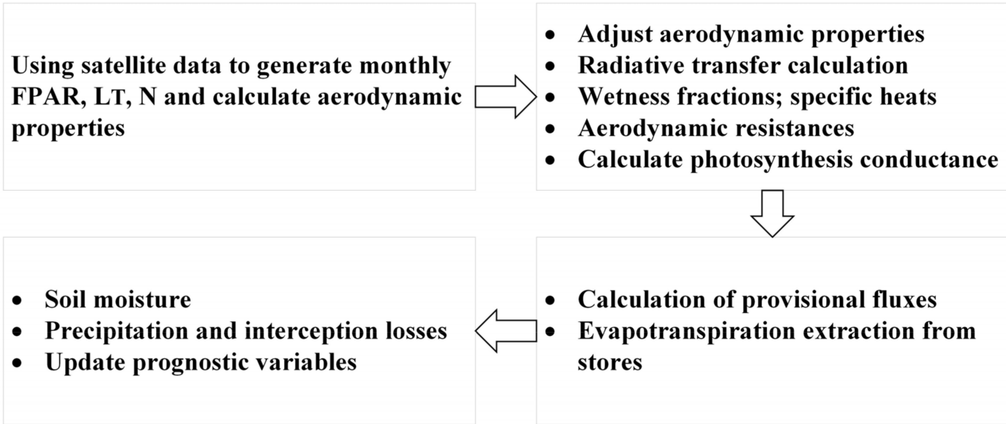

Figure 3. The simulation process of SiB2.

First, vegetation parameters such as canopy photosynthetic active radiation ($FPAR$), vegetation cover index (VCI), leaf area index (L_T) and green canopy percentage (N) are generated, which vary dynamically with time. They are closely associated with the normalized vegetation index (NDVI). $FPAR$ is calculated by:

$$FPAR = \frac{(SR - SR_{i,min})(FPAR_{max} - FPAR_{min})}{SR_{i,max} - SR_{i,min}} + FPAR_{min} \tag{2}$$

$$SR = \frac{1 + NDVI}{1 - NDVI} \tag{3}$$

where $FPAR_{max}$ and $FPAR_{min}$ are taken as 0.950 and 0.001, respectively. $FPAR_{max}$ and $FPAR_{min}$ are independent of the vegetation type, and i is the vegetation type, $SR_{i,max}$ and $SR_{i,min}$ are SR values corresponding to 98 and 5% of NDVI values distribution, respectively.

The green leaf area index L_g is as follows:

$$L_g = (1 - F_{cl})L_{g,i,max}\frac{log(1 - FPAR)}{log(1 - FPAR_{max})} + F_{cl}\frac{L_{g,i,max}FPAR}{FPAR_{max}} \tag{4}$$

where, F_{cl} is the proportion of clumped vegetation in the grid area and $L_{g,i,max}$ is the maximum green leaf area index of vegetation. The leaf area index L_T is the sum of vegetation stem area index, green leaf area index and dead leaf area index.

$$L_T = L_s + L_d + L_g \tag{5}$$

where, L_s is stem area index, L_d is dead leaf area index.

The green ratio of the canopy (N) is expressed as:

$$N = {}^{L_g}/_{L_T} \tag{6}$$

where,

$$L_d = L_{g_{n-1}} - L_{g_n},\ L_d \geq 0 \tag{7}$$

The morphological parameters of the vegetation and the length of the ground roughness are input into the SiB2 parameter program to finally obtain the air roughness ($Z0$), the zero-surface displacement of the plants (D), the overall boundary layer impedance coefficient ($C1$), the impedance coefficient between the soil and plant layers ($C2$), and the canopy heating height (ha) for different vegetation types.

Second, after the above offline data and parameters are set up, it will move to online analysis, such as Adjust aerodynamic properties. In this process, latent heat flux will be generated. It is the sum of the latent heat flux between vegetation canopy and canopy air and the latent heat flux between bare ground and canopy air, which is calculated as follows:

$$\lambda E = \lambda E_{ct} + \lambda E_{gs} \quad (8)$$

where, λE is the latent heat flux, λE_{ct} is the canopy latent heat flux, λE_{gs} is the latent heat flux on bare ground surface. λE_{ct} is calculated as:

$$\lambda E_{ct} = \left[\frac{e^*(T_c) - e_a}{r_c + 2r_b}\right]\frac{\rho c_p}{\gamma} \quad (9)$$

λE_{gs} is calculated as:

$$\lambda E_{gs} = \left[\frac{h_{soil}e^*(T_g) - e_a}{r_{soil} + r_d}\right]\frac{\rho c_p}{\gamma} \quad (10)$$

where, T_c, T_g = canopy, soil surface temperature, respectively, (K); $e^*(T_c)$, $e^*(T_g)$ = saturated vapor pressure at temperature T_c and T_g (Pa), respectively; e_a = canopy air space vapor pressure (Pa); ρ, c_p = density, specific heat of air, respectively (kg/m, J/kg/K); γ = psychrometric constant (Pa/K); λ = latent heat of vaporization; r_c = bulk stomatal resistance of upper-story vegetation (s/m); r_c = bulk canopy boundary layer resistance (s/m); h_{soil} = relative humidity within pore space of surface soil layer; r_{soil} = bare soil surface resistance (s/m); r_d = aerodynamic resistance between ground and canopy air space (s/m).

Finally, the ET is converted from latent heat fluxes:

$$ET = \frac{(e_a - e_r)}{\lambda r_a} \times \frac{\rho c_p}{\gamma} \quad (11)$$

where, $\lambda = (3150.19 - 2.378 \times T_m) \times 1000$, T_m is the temperature at the reference height. r_a is aerodynamic resistance between canopy air space and reference height (s/m).

4. Results

4.1. Simulation Results Validation

We established an initialized parameter scheme for the study area based on the data in the references and the climatic characteristics of the upper Minjiang River (Appendix A Table A7) and input the forcing variables required for SiB2 to simulate the hour-by-hour ET in 2013. To verify the accuracy of SiB2 at the daily scale, the 3-hourly step-by-step calculation results of SiB2 were combined into daily ET, and the simulated results for February, May, August, and November 2013 during the vegetation growth period were selected for comparison with the daily ET observations at the meteorological station in Lixian during the corresponding time periods (as shown in Figure 4). On about half of the days in February and May, the simulated values were larger than the observed values, while on about 80% of the days in August and November, the simulated values were smaller than the actual measured values in the evaporation dishes. The correlation coefficients between the simulated and actual observed values for February, May, August, and November are 0.708, 0.747, 0.58, and 0.637, respectively (all significant with p-values < 0.05). As can be seen from the figure, the simulated results were consistent with the trend of the observed values of evapotranspiration from the evaporation dishes. The simulated and measured values of the four months were analyzed separately by one-sided T-test, and the differences between simulated and measured values were not significant in February and May (p-values 0.24 and 0.16, respectively), while the differences between simulated and measured values were significant in August and November (p-values < 0.05). Since the results of SiB2 simulations were averaged over the pixels where the stations were located, the observation scale may be a potential reason for the discrepancy between the simulated and measured values.

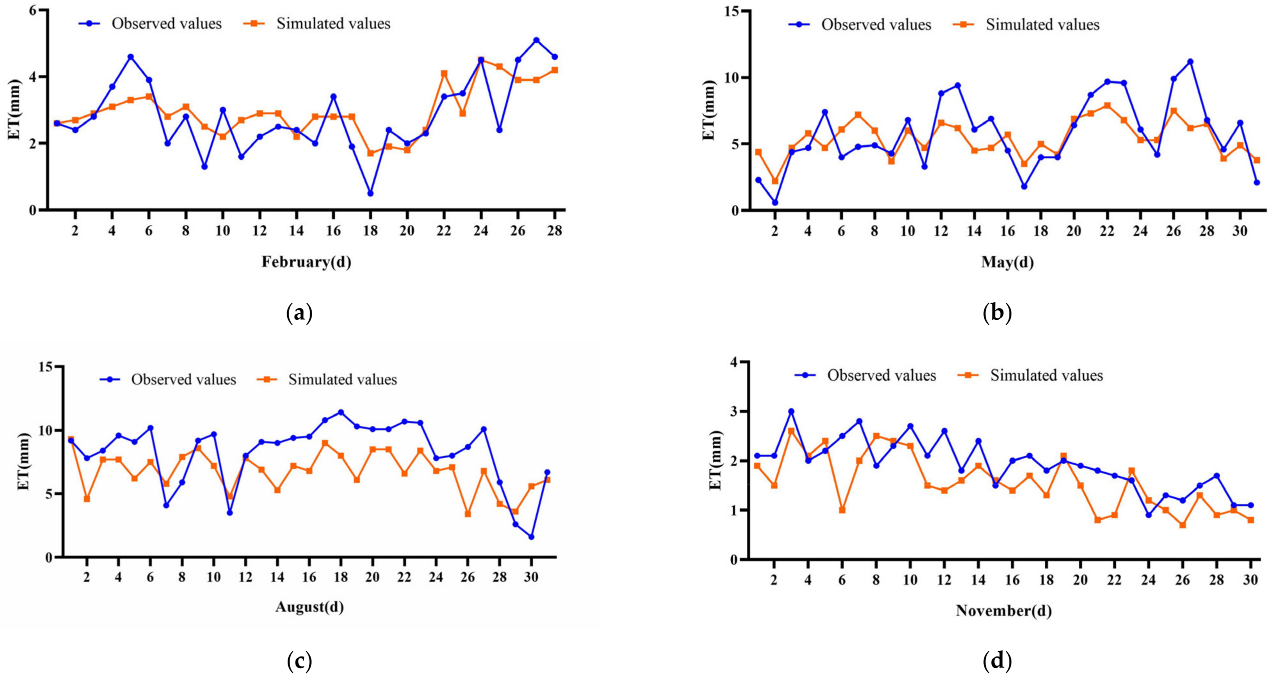

Figure 4. Comparison of simulated and observed values. (**a**–**d**) are the observed and simulated values in February, May, August, and November, respectively.

To test the accuracy of the model results on the monthly scale, we compared the monthly simulated ET of SiB2 and the measured ET by evaporation dishes at the meteorological station in Lixian. Figure 5a shows that the monthly simulated ET is generally smaller than the measured ET, and the relative errors between the two range from 1.48% to 20.72%. Since the measured ET was influenced by the environment, if the wind speed was higher, the measured ET would be higher than the actual ET, which may be the reason for the large relative errors between the simulated and measured results. Figure 5b shows a comparison of the monthly accumulation of simulated and measured values. Although the simulated errors may be larger in some months, the cumulative errors were smaller on monthly or seasonal time scales. The annual simulated total ET was 1469.1 mm and the annual measured total ET 1579.5 mm, with a relative error of 6.99%. Overall, the simulated results of SiB2 correlate well with the measured results, indicating the feasibility of SiB2 in the study area.

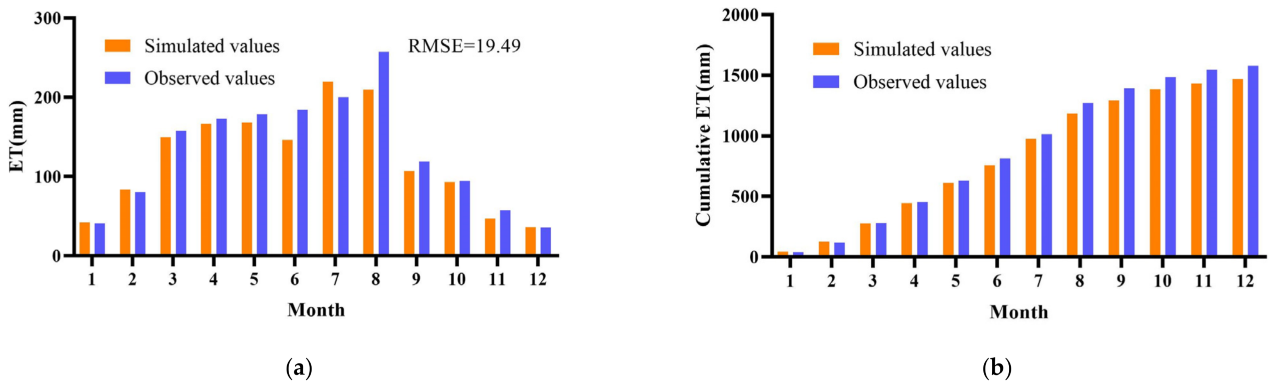

Figure 5. Comparison of simulated and observed values. (**a**) is the monthly simulated and measured ET. (**b**) is the monthly accumulation of simulated and measured ET.

4.2. Temporal Variation in Vegetation ET

4.2.1. Daily Characteristics in Vegetation ET

Figure 6a–d shows the daily ET for each type of vegetation from 1 to 10 February (winter), 1 to 10 May (spring), 1 to 10 August (summer), and 1 to 10 November (autumn), respectively.

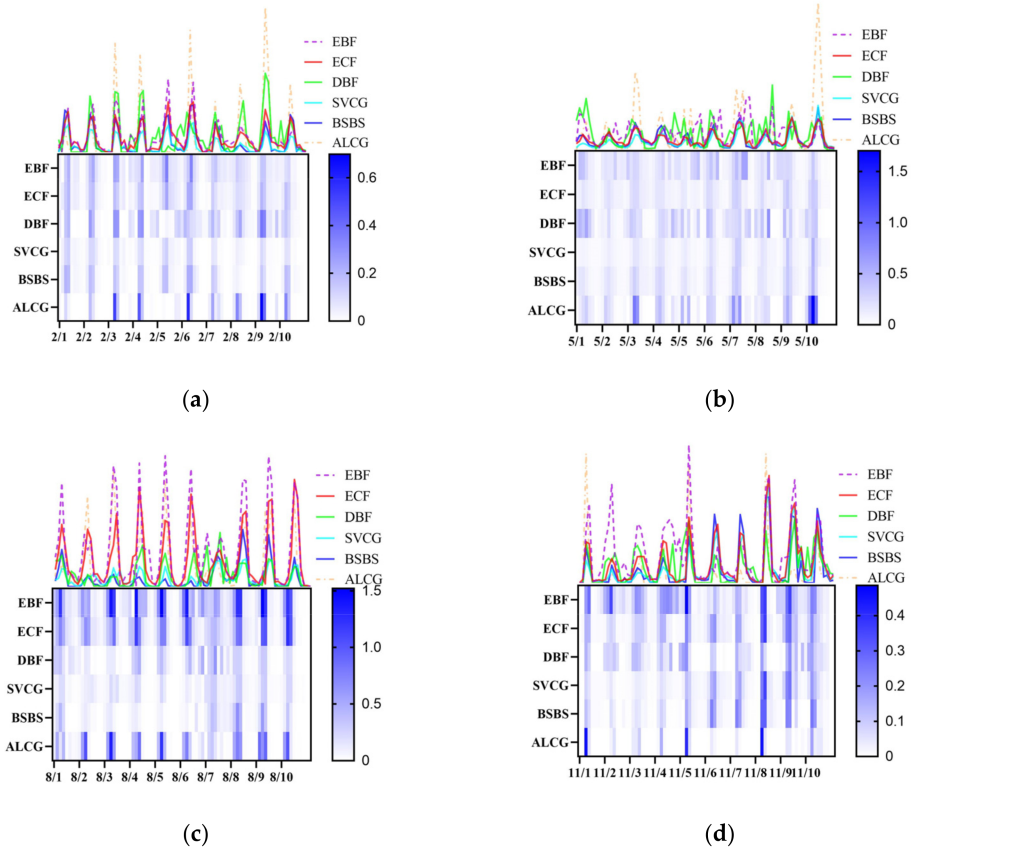

Figure 6. Daily ET for six type of vegetation. (**a**–**d**) are the daily ET of the EBF, ECF, DBF, SVCG, BSBS, ALCG in February, May, August and November, respectively.

In February, daily ET was relatively small for all vegetation types (Figure 6a), with the maximum ET occurring between 9 a.m. and 12 p.m. SVCG has the smallest variation in daily ET, and its peak within a single day is 0.17 mm/h. This may be due to the weak vegetation transpiration during the non-growing season, when most of the grassland is in a dead state. The ET curves of the remaining vegetation types were multi-peaked and irregular in a single day. During this period, the maximum average daily ET was 1.81 mm/d for EBF and the minimum average daily ET was 1.16 mm/d for SVCG. In May, the magnitude of daily ET was similar for all vegetation types except for SVCG, which had a smaller daily ET (Figure 6b). During this period, DBF had the highest average daily ET (6.24 mm/d) and SVCG the lowest (2.14 mm/d). the average daily ET of EBF (4.47 mm/d) and BSBS was relatively similar (4.43 mm/d). In August, daily ET was generally high for all vegetation types (Figure 6c), with the highest peak daily ET for EBF, DBF and ECF. During this period, EBF had the highest average daily ET (9.64 mm/d), which was relatively close to DBF (9.57 mm/d), and SVCG had the lowest average daily ET (3.62 mm/d). In November, the peak daily ET was smaller for all vegetation types (Figure 6d), and SVCG and ALCG had the lowest daily ET, with relatively similar average daily ET values, probably because most of the agricultural fields in the study area were paddy fields and were harvested during this period. Similar to SVCG, ET was mostly surface evaporation. The highest average daily ET (2.38 mm/day) was observed in EBF, and the lowest average daily ET (0.95 mm/day) was observed in SVCG during this period.

4.2.2. Seasonal Variation in the ET in Dominant Vegetation

The main vegetation types in the upper Minjiang River were SVCG, ECF and BSBS, which account for 35.72%, 30.71% and 25.66% of the study area, respectively, and had a significant influence on the ET pattern. Figure 7a shows the monthly average ET values for each vegetation type in the study area. After summing up the months on an annual scale (as shown in Figure 7b), the magnitude of annual ET was in the order of BSBS (988.56 mm) > ECF (984.37 mm) > SVCG (846.74 mm). During the growing season, the sum of monthly ET was in the order of ECF (623.5 mm) > BSBS (622.06 mm) > SVCG (510.11 mm) and they accounted for 63.34%, 62.93% and 60.24% of the total ET, respectively. The ET reached its peak in summer, and the sum of monthly ET in summer was ECF (376.13 mm) > BSBS (372.16 mm) > SVCG (302.63 mm) in order, and they accounted for 60.33%, 59.83% and 59.33% of the total ET during the growing season and 38.21%, 37.65% and 35.74% of the total annual ET, respectively. During the non-growing season, the sum of monthly ET was BSBS (366.5 mm) > ECF (360.87 mm) > SVCG (336.63 mm) in order, and they accounted for 37.07%, 36.66% and 39.76% of the total annual ET, respectively. To sum up, the vegetation evapotranspiration in the upper Minjiang River region showed obvious seasonal variations. During the growing season, the ET was larger due to the strong transpiration of vegetation, and accounted for more than 58% of the total annual ET; during the non-growing season, the ET was smaller, and accounted for less than 40% of the total annual ET.

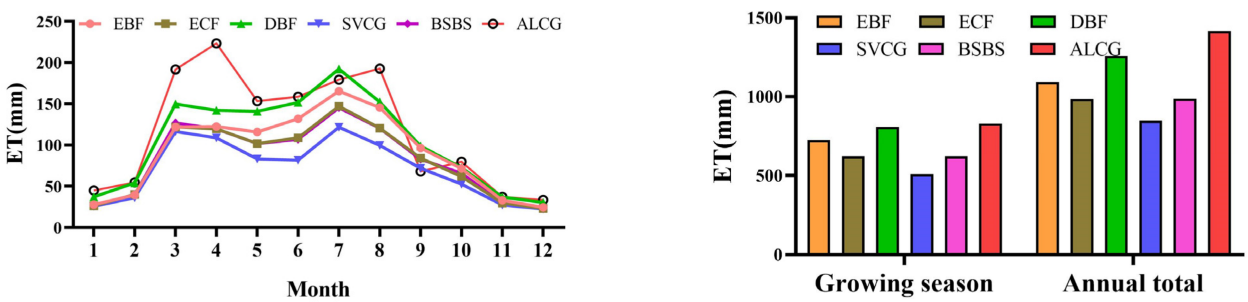

(**a**) (**b**)

Figure 7. Seasonal dynamics of ET for different vegetation. (**a**) is the monthly ET of the six vegetation types. (**b**) is the sum of the monthly ET of the six vegetation types for the growing season and in a year.

4.3. Spatial Variation in ET

Figure 8a–l shows the spatial distribution of the average daily ET for each month using the natural breaks method. The daily ET in the upper Minjiang River was small in winter, with the average daily ET of 0.87 mm and 1.4 mm in January and February, respectively, and 0.97 mm and 0.76 mm in November and December, respectively. The average daily ET was more vigorous from March to October, peaked in July, and then declined (as shown in Figure 9).

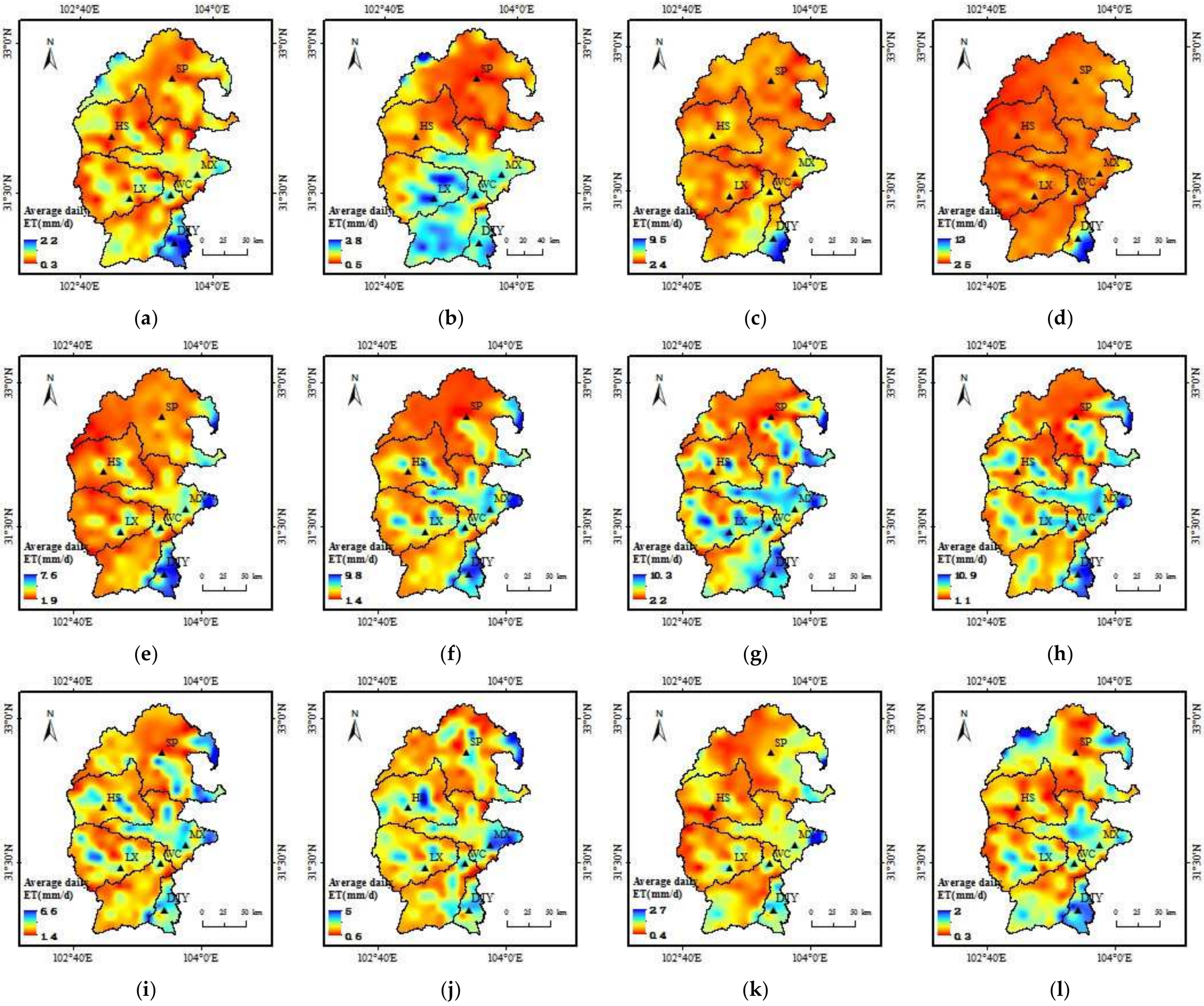

Figure 8. Spatial and temporal of ET in six counties. (**a**–**l**) are the average daily ET in six counties.

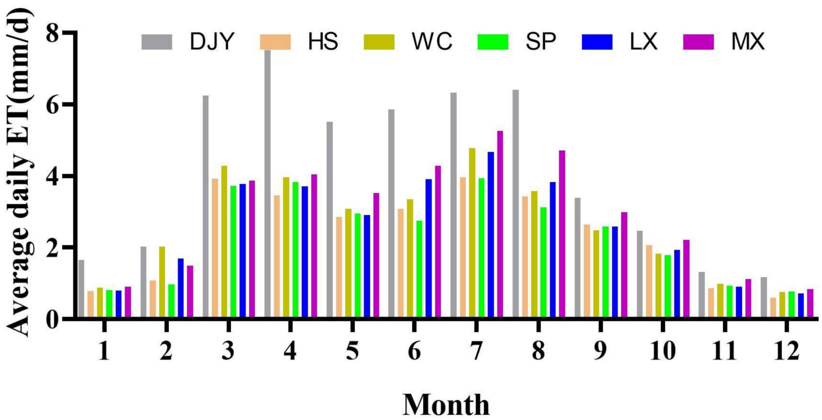

Figure 9. The sum of the average daily ET for each county in 12 months.

In the six counties, DJY had the highest average daily ET (6.42 mm/d) in spring. There was no significant difference in the average daily ET of the remaining five counties (the average daily ET was 3.33 mm/d), with the highest being MX (3.67 mm/d) and the smallest being HS (3.13 mm/d). In summer, the average daily ET of DJY was 6.2 mm/d, while the average daily ET of the other five counties was 3.82 mm/d, with the highest being MX (4.75 mm/d) and the lowest being SP (3.27 mm/d). In autumn, the average daily ET decreased significantly in all counties, and the average daily ET in DJY was 2.39 mm/d, while the average daily ET in the remaining five counties was 1.86 mm/d. In winter, the average daily ET in DJY was 1.62 mm/d, while the average daily ET in the remaining five counties was 1.01 mm/d. Among the five counties of HS, SP, WC, MX and LX, MX had the highest average daily ET in spring and summer, and the vegetation distribution in its territory was mostly evergreen coniferous forest, evergreen broad-leaved shrub forest and deciduous broad-leaved shrub forest, and its temperature was also higher. Overall, the average daily ET was higher in spring and summer with little variation, and it was smaller in autumn and winter with less fluctuation between the two seasons. The highest regional average temperature, lowest elevation, and more distribution of water bodies may explain the higher ET in DJY.

In terms of elevation (as shown in Table 1), the variation in ET in the study area decreases with increasing elevation. The key point where ET decreases sharply is at 3000 m. This may be related to the elevation distribution of vegetation in the upper Minjiang River. Forests are concentrated below 3000 m, while shrubs and meadows are mainly distributed above 3000 m, and their ET characteristics are different from those of forests. In addition, the temperature and other hydrothermal conditions change significantly with increasing elevation, leading to significant changes in ET in areas above 3000 m.

Table 1. Variation in ET with elevation (mm).

Elevation	January	February	March	April	May	June	July	August	September	October	November	December	Annual ET
[500,1000)	58	61	227	267	178	181	196	215	105	79	41	40	1648
[1000,1500)	51	60	170	157	174	191	221	211	114	106	51	38	1544
[1500,2000)	35	57	154	128	123	138	180	143	87	81	34	28	1188
[2000,2500)	31	51	140	124	121	139	181	141	95	79	32	25	1159
[2500,3000)	29	48	127	128	115	132	169	147	95	71	33	27	1121
[3000,3500)	24	33	124	124	96	95	130	103	80	63	29	22	923
[3500,4000)	25	34	116	106	82	81	124	98	75	51	26	23	841
[4000,4500)	24	32	104	100	77	74	116	94	66	48	27	20	782
[4500,6000)	19	34	96	90	70	67	94	74	54	39	22	16	675

4.4. Correlation of ET with Environmental Factors

At the annual scale, SiB2 results showed significant correlations with temperature and elevation, 0.785 and 0.733, respectively, and weaker correlations with precipitation, with correlation coefficients below 0.36. At the monthly scale, the correlations between ET and elevation, temperature and precipitation of the study area in 2013 are shown in Figure 10. The correlation between ET and air temperature and elevation gradually decreased from the growing season, while the correlation between ET and precipitation was weak and fluctuated greatly. In November and December, the correlations between ET and air temperature, elevation, and precipitation tended to be close.

Figure 11 shows the dynamics of ET and precipitation, temperature and the correlations for the six counties. In Figure 11a–g, the temperature shows a single-peaked pattern, with a sharp increase in the study area in March and April. However, the ET exhibited a double-peak pattern. The correlation coefficients between ET and air temperature for each county ranged from 0.772 to 0.919. Among these counties, DJY has the lowest correlation coefficient between ET and air temperature. Compared with air temperature, the correlations between ET and precipitation were lower at 0.529–0.773 (as shown Figure 11h–l). From the simulation results, the ET in the non-growing season was less than the precipitation. Among them, the ET in HS and SP counties was greater than precipitation in summer. Similar to air temperature, the correlation between ET and precipitation was the lowest in DJY.

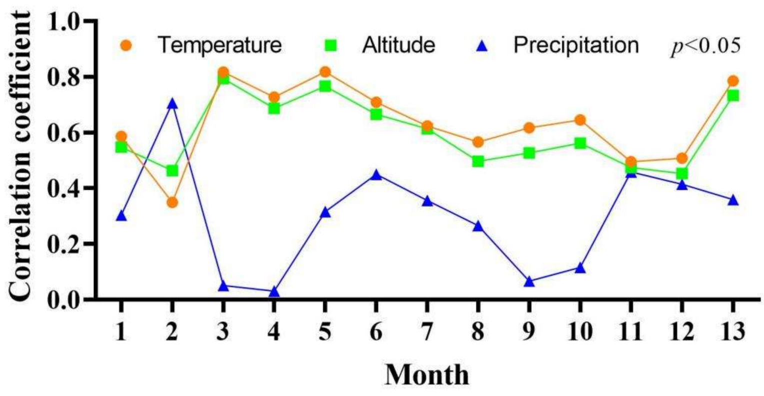

Figure 10. Correlation of ET with temperature, altitude and precipitation.

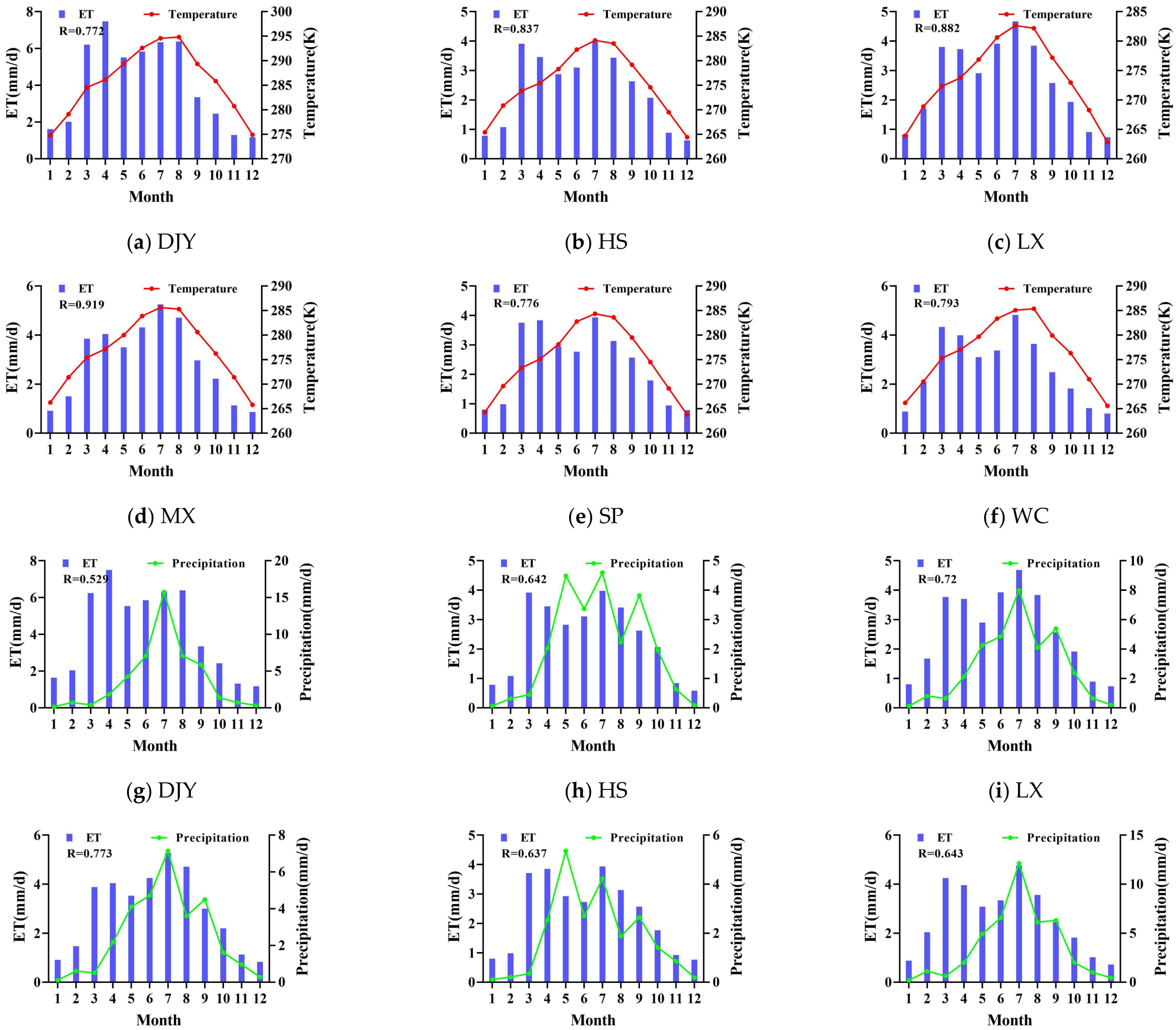

(**a**) DJY (**b**) HS (**c**) LX

(**d**) MX (**e**) SP (**f**) WC

(**g**) DJY (**h**) HS (**i**) LX

(**j**) MX (**k**) SP (**l**) WC

Figure 11. Correlation of daily average ET with temperature and precipitation for the simulated months. (**a**–**f**) are the correlations of daily average ET with temperature for DJY, HS, LX, MX, SP, and WC counties, respectively; (**g**–**l**) are the correlations of daily average ET with precipitation for DJY, HS, LX, MX, SP, and WC counties.

5. Discussion

From the comparison of the simulated and observed ET, the difference between the two was not significant in the early stage of the simulation but it was significant in the later stage of the simulation at the intra-annual scale, but the two were still well correlated. The difference in scales between simulations and observations was a factor for the significant difference in the later stage.

The annual difference in temperature in the upper Minjiang River was small, with a rapid rise in temperature in spring and a rapid fall in autumn, making a clear distinction between wet and dry seasons. The areas with high ET in spring were mainly concentrated in low elevation counties such as DJY. Surface temperatures in these areas were relatively high, and crops and water bodies were widely distributed. The high ET may be due to the fact that the snow melted in the early spring when the temperature just rose above 0 °C. In May, the ET gradually increased in the sub-basins of Mogunao and Heishui with the gradual increase in surface temperature. The evergreen coniferous forest, evergreen broadleaf forest, deciduous broadleaf forest, evergreen broadleaf shrub forest and deciduous broadleaf shrub forest distributed in these sub-basins may be one of the potential reasons for the higher daily ET. During summer, the ET showed high values throughout the study area. Into early autumn, the ET in the study area remained at a high level, with the distribution of high and low value areas close to that of summer. By November, the ET declined sharply in all areas except for slightly higher ET in the eastern part of the study area at lower elevations. Despite the low ET of the agricultural fields in winter, the unique topographic and climatic conditions made DJY the highest ET of all regions.

The distribution of ET in the upper Minjiang River was uneven within one year. The multi-year average ET showed a trend of gradual decrease from southeast to northwest, and the spatial variation in ET in DJY was large [34]. Our simulation results were consistent with this study in terms of spatial trends. However, the annual ET obtained from the observation station in Lixian and the simulation results of SiB2 also found that the annual ET of all vegetation types were greater than the results of Fu Baopu model [34]. The upper Minjiang River afforestation and forest conservation program was initiated in 1998 and increased forest cover to 34% by 2006 [41]. After reforestation, trees were in a rapid growth phase [42], which, combined with lack of management and rising air temperatures, may lead to an increase in ET [43].

Whether regional-scale ET estimates are based on remote sensing models or surface process models, their validation at the regional scale is a challenge. This requires detailed observations of the surface property fields at the regional scale. In this study, the simulation results were only validated locally at the point scale. Future evaluations of SiB2 ET simulations in mountainous areas will seek data from large-aperture scintillators. At present, the applications of land surface process models are mostly in flat terrain areas, and the applicability of SiB2 in mountainous areas has not been well investigated. Improving the SiB2 model based on DEM data and considering the influence of topographic factors on water-heat exchange will included in future work to simulate ET in mountainous areas.

6. Conclusions

In this study, the spatial and temporal variation in ET in the upper Minjiang River was simulated using the SiB2 model with the Chinese regional surface meteorological element dataset as the data source, and its correlation with temperature, elevation and precipitation was analyzed. (1) The simulated results of ET by the SiB2 model in the study area are validated at the daily, monthly, and annual scales, respectively. At the daily scale, the simulated ET is generally smaller than the measured ET. At the monthly scale, the relative errors between the simulated and measured values varies from 1.48% to 20.72%. The relative error between the simulated and measured values of total annual ET is 6.99%. The application of the SiB2 model in the study area is feasible. (2) The ET dynamics of different vegetation in the upper Minjiang River are analyzed. At the daily scale, each vegetation shows obvious daily variation characteristics, and there are obvious seasonality of daily ET, with smaller daily ET in February and November (non-growing season) and larger daily ET in May and August (growing season). At the monthly scale, the vegetation ET in the upper Minjiang River shows obvious seasonal variation with the change in climate. The growing season ET accounts for more than 58% of the total annual ET, and the non-growing season ET accounts for less than 40% of the total annual ET. (3) The spatial and temporal characteristics of ET in the study area are analyzed. The ET is higher in areas with more intensive growth of crops and at lower elevations. In the whole study area, the ET is highest in spring and summer, followed by autumn, and is the lowest in winter.

Author Contributions: Conceptualization, methodology, software, B.K. and X.L.; writing—original draft preparation, data curation, X.L.; investigation, formal analysis, validation, visualization, B.H.; writing—review and editing, B.H. and B.K.; supervision, project administration, funding acquisition, H.Y. and B.K. All authors have read and agreed to the published version of the manuscript.

Funding: This research was funded by the National Natural Science Foundation of China (No. 41871357, 41971226), Shenzhen Fundamental Research Program (No. JCYJ20190812171419161), National Basic Research Program of China (2017YFC1503103) and the Strategic Priority Research Program of the Chinese Academy of Sciences (XDA19030303, XDA28110503).

Institutional Review Board Statement: Not available.

Informed Consent Statement: Not available.

Data Availability Statement: The China Meteorological Forcing Dataset is available from https://data.tpdc.ac.cn/en/data/7a35329c-c53f-4267-aa07-e0037d913a21/, accessed on 1 June 2022. The Shuttle Radar Topography Mission data sets are available from https://www.resdc.cn/data.aspx?DATAID=284, accessed on 1 June 2022. The Chinese soil data set based on world soil database (hwsd) (v1.1) are available from http://www.ncdc.ac.cn/portal/metadata/a948627d-4b71-4f68-b1b6-fe02e302af09. The NDVI is available from https://www.resdc.cn/DOI/doi.aspx?DOIid=50, accessed on 1 June 2022.

Conflicts of Interest: The authors declare no conflict of interest.

Appendix A

Table A1. All data sets used and their sources.

Datasets	Sources
CMFD (China Meteorological Forcing Dataset)	http://www.tpdc.ac.cn/zh-hans/data/7a35329c-c53f-4267-aa07-e0037d913a21/ (accessed on 20 April 2020)
SRTM (Shuttle Radar Topography Mission)	https://www.resdc.cn/data.aspx?DATAID=284 (accessed on 20 April 2020)
Chinese soil data set based on world soil database (hwsd) (v1.1)	http://www.ncdc.ac.cn/portal/metadata/a948627d-4b71-4f68-b1b6-fe02e302af09 (accessed on 20 April 2020)
LULC (Land use/Land cover)	http://www.tpdc.ac.cn/zh-hans/data/f1aaacad-9f42-474e-8aa4-d37f37d6482f/ (accessed on 20 April 2020)
NDVI	https://www.resdc.cn/DOI/doi.aspx?DOIid=50 (accessed on 20 April 2020)

Table A2. Mapping between LULC vegetation types and SiB2 vegetation types.

LULC Vegetation Types	SiB2 Vegetation Types
Evergreen Broadleaf Forest	Evergreen Broadleaf Forest
Deciduous Broadleaf Forest	Deciduous Broadleaf Forest
Evergreen Coniferous Forest, Mixed Coniferous Forest	Evergreen Coniferous Forest
Grasslands, Herbaceous Marshes, Meadows	Short Vegetation/C4 Grassland
Deciduous Broad-leaved Shrub Forests, Sparse Shrub Forests	Broadleaf Shrubs on Bare Soil
Paddy Field, Dry Land, Grass	Agricultural Land/C3 Grassland

Table A3. Vegetation morphological parameters.

Morphological Parameters Related to Vegetation Type							
Morphological parameters	Symbol	Vegetation type					
		1	2	4	6	7	9
Top height of crown (m)	Z_2	35.0	20.0	17.0	1.0	0.5	1.0
Height of crown base (m)	Z_1	1.0	11.5	8.5	0.1	0.1	0.1
Leaf density bending height (m)	Z_c	28.0	17.0	10.0	0.55	0.3	0.55
Canopy coverage ratio (%)	V	1.0	1.0	1.0	1.0	0.1	1.0
Foliar angle distribution factor	χ_L	0.1	0.25	0.01	−0.3	0.01	−0.3
Leaf width (m)	l_W	0.05	0.08	0.001	0.01	0.003	0.01
Leaf length (m)	l_l	0.1	0.15	0.055	0.3	0.03	0.3
Soil depth (m)	D_T	3.5	2.0	2.0	1.5	1.5	1.5
Root depth (m)	D_r	1.5	1.5	1.5	1.0	1.0	1.0
Morphological parameters not related to vegetation type							
Morphological parameters	Symbol	Value					
Ground roughness length (m)	Z_s	0.05					
Momentum transfer parameter increase factor	G_1	1.449					
Momentum transfer parameter height conversion factor	G_4	11.785					
Depth of topsoil layer (m)	D_1	0.02					

Table A4. Vegetation optical properties parameters.

	Optical Properties Parameters	**Symbol**	**Vegetation Type**					
			1	**2**	**4**	**6**	**7**	**9**
Living Plants	Foliar reflectance in the visible wavelength band	$\alpha_{V,l}$	0.1	0.1	0.07	0.105	0.1	0.105
	Foliar reflectance in the near-infrared band	$\alpha_{N,l}$	0.45	0.45	0.35	0.58	0.45	0.58
	Transmission in the visible wavelength band	$\delta_{V,l}$	0.05	0.05	0.05	0.07	0.05	0.07
	Transmission in the near-infrared band	$\delta_{N,l}$	0.25	0.25	0.1	0.25	0.25	0.25
Dead plants	Foliar reflectance in the visible wavelength band	$\alpha_{V,d}$	0.16	0.16	0.16	0.36	0.16	0.36
	Foliar reflectance in the near-infrared band	$\alpha_{N,d}$	0.39	0.39	0.39	0.58	0.39	0.58
	Transmission in the visible wavelength band	$\delta_{V,d}$	0.001	0.001	0.001	0.22	0.001	0.22
	Transmission in the near-infrared band	$\delta_{N,d}$	0.001	0.001	0.001	0.38	0.001	0.38
Soil	Visible wavelength reflectance	α_{sV}	0.11	0.11	0.11	0.11	0.11	0.1
	Near-infrared band reflectance	α_{sN}	0.225	0.225	0.225	0.225	0.225	0.15

Table A5. Vegetation physiological parameters.

Physiological Parameters Related to Vegetation Type							
Physiological parameters	Symbol	Vegetation type					
		1	2	4	6	7	9
The catalytic rate of photosynthesis RuBisCO ($mol \cdot m^{-2} \cdot s^{-1}$)	V_{max0}	1×10^{-4}	1×10^{-4}	4×10^{-5}	3×10^{-5}	6×10^{-5}	1×10^{-4}
Parameters of internal quantum effects of photosynthesis (mol mol^{-1})	ε	0.08	0.08	0.08	0.05	0.08	0.08
Stomatal slope factor	m	9.0	9.0	9.0	4.0	9.0	9.0
Minimum stomatal conductivity(mol $m^{-2}s^{-1}$)	b	0.01	0.01	0.01	0.04	0.01	0.01
Photosynthetic coupling factor	β_{ce}	0.98	0.98	0.98	0.8	0.98	0.98
High temperature shear factor in photosynthesis (K)	S_2	313	311	303	313	313	308
Low temperature shear factor in photosynthesis (K)	S_4	288	283	278	288	283	281
Semi-obstructed water potential parameters (m)	ψ_c	−200	−200	−200	−200	−200	−200
Leaf respiration impact factor	f_d	0.015	0.015	0.015	0.025	0.015	0.015
Physiological parameters not related to vegetation type							
Physiological parameters	Symbol	Value					
RuBisCO catalytic capacity for CO_2 fixation (Pa)	S	2600×0.57^{Q_t}					
Michaelis-Memen constants for CO_2 by RuBisCO (Pa)	K_c	30×2.1^{Q_t}					
The inhibition constants for O_2 by RuBisCO (Pa)	K_o	$30,000 \times 1.2^{Q_t}$					
Photosynthetic coupling factor	β_{ps}	0.95					
High temperature shear factor in photosynthesis (K)	S_1	0.3					
Low temperature shear factor in photosynthesis (K)	S_3	0.2					
High temperature shear factor in respiration (K)	S_5	1.3					
High temperature shear factor in respiration (K)	S_6	328					
Q_{10} temperature factor	Q_t	$(T_c - 298)/10$					

Table A6. Soil properties parameters.

Soil Properties Parameters	Symbol	Soil Type				
		1	2	3	4	5
Soil moisture index	B	4.05	4.90	5.39	7.12	8.52
Soil water potential	ψ_s	−0.04	−0.07	−0.15	−0.12	−0.36
Saturated water conductivity (m s^{-1})	$K_s \times 10^6$	176.0	35.0	7.0	6.3	2.5
Soil porosity (%)	θ_s	0.40	0.44	0.45	0.42	0.48

Table A7. Initial parameters of SiB2.

Initialization Parameters	Vegetation Type					
	1	2	4	6	7	9
Reference height temperature (K)	263.0	263.0	263.0	263.0	263.0	263.0
Reference height (m)	45.0	45.0	45.0	2.0	2.0	2.0
Vegetation temperature (K)	262.0	262.0	262.0	262.0	262.0	262.0
Canopy air temperature (K)	262.0	262.0	262.0	262.0	262.0	262.0
Surface temperature (K)	265.0	265.0	265.0	265.0	265.0	265.0
Deep earth temperature (K)	262.0	262.0	262.0	262.0	262.0	262.0
Soil surface layer moisture (%)	0.4	0.4	0.4	0.4	0.4	0.65
Root domain humidity (%)	0.4	0.4	0.4	0.4	0.4	0.7
Exchange domain humidity (%)	0.4	0.4	0.4	0.4	0.4	0.6

References

1. Li, A.; Yin, G.; Jin, H.; Bian, J.; Zhao, W. Principles and methods for the retrieval of biothysical variables in mountainous areas. *Remote Sens. Technol. Appl.* **2016**, *31*, 1–11.
2. Brutsaert, W. *Hydrology: An Introduction*; Cambridge University Press: Cambridge, UK, 2005.
3. Stefanidis, S.; Alexandridis, V. Precipitation and potential evapotranspiration temporal variability and their relationship in two forest ecosystems in Greece. *Hydrology* **2021**, *8*, 160. [CrossRef]
4. Long, D.; Singh, V.P. Integration of the GG model with SEBAL to produce time series of evapotranspiration of high spatial resolution at watershed scales. *J. Geophys. Res.* **2010**, *115*, D21128. [CrossRef]
5. McCabe, M.F.; Wood, E.F. Scale influences on the remote estimation of evapotranspiration using multiple satellite sensors. *Remote Sens. Environ.* **2006**, *105*, 271–285. [CrossRef]
6. Priestley, C.H.B.; Taylor, R.J. On the assessment of surface heat flux and evaporation using large-scale parameters. *Mon. Weather Rev.* **1972**, *100*, 81–92. [CrossRef]
7. Shen, Y.; Kondoh, A.; Tang, C.; Zhang, Y.; Chen, J.; Li, W.; Sakura, Y.; Liu, C.; Tanaka, T.; Shimada, J. Measurement and analysis of evapotranspiration and surface conductance of a wheat canopy. *Hydrol. Processes* **2002**, *16*, 2173–2187. [CrossRef]
8. Bowen, I.S. The ratio of heat losses by conduction and by evaporation from any water surface. *Phys. Rev.* **1925**, *27*, 779–787. [CrossRef]
9. Swinbank, W.C. The measurement of vertical transfer of heat and water vapor by eddies in the lower atmosphere. *J. Meteorol.* **1951**, *8*, 135–145. [CrossRef]
10. Wang, T.; Ochs, G.R.; Clifford, S.F. A saturation-resistant optical scintillometer to measure Cn2. *J. Opt. Soc. Am.* **1978**, *68*, 334–338. [CrossRef]
11. Yonaba, R.; Biaou, A.C.; Koïta, M.; Tazen, F.; Mounirou, L.A.; Zouré, C.O.; Queloz, P.; Karambiri, H.; Yacouba, H. A dynamic land use/land cover input helps in picturing the Sahelian paradox: Assessing variability and attribution of changes in surface runoff in a Sahelian watershed. *Sci. Total Environ.* **2020**, *25*, 143792. [CrossRef]
12. Bastiaanssen, W.; Menenti, M.; Feddes, R.; Holtslag, A.A.M. A remote sensing surface energy balance algorithm for land(SEBAL).1.Formulation. *J. Hydrol.* **1998**, *212*, 198–212. [CrossRef]
13. Su, Z. The Surface Energy Balance System (SEBS) for estimation of turbulent heat fluxes. *Hydrol. Earth Syst. Sci. Discuss.* **2002**, *6*, 85–100. [CrossRef]
14. Allen, R.G.; Tasumi, M.; Trezza, R. Satellite-based energy balance for mapping evapotranspiration with internalized calibration (METRIC)-Model. *J. Irrig. Drain. Eng.* **2007**, *133*, 380–394. [CrossRef]
15. Norman, J.M.; Kustas, W.P.; Humes, K.S. Source approach for estimating soil and vegetation energy fluxes in observations of directional radiometric surface temperature. *Agric. For. Meteorol.* **1995**, *77*, 263–293. [CrossRef]
16. Roerink, G.J.; Su, Z.; Menenti, M. S-SEBI: A simple remote sensing algorithm to estimate the surface energy balance. *Phys. Chem. Earth Part B Hydrol. Ocean. Atmos.* **2000**, *25*, 147–157. [CrossRef]

17. Chen, X.; Su, Z.; Ma, Y.; Yang, K.; Wang, B. Estimation of surface energy fluxes under complex terrain of mt. qomolangma over the tibetan plateau. *Hydrol. Earth Syst. Sci. Discuss.* **2012**, *9*, 10411–10445. [CrossRef]
18. Penman, H. Natural evaporation from open water, bare soil, and grass. *Proceeding R. Soc. A* **1948**, *193*, 120–146. [CrossRef]
19. Miralles, D.G.; De Jeu, R.A.; Gash, J.H.; Holmes, T.R.; Dolman, A.J. Magnitude and variability of land evaporation and its components at the global scale. *Hydrol. Earth Syst. Sci.* **2011**, *15*, 967–981. [CrossRef]
20. Mu, Q.; Heinsch, F.A.; Zhao, M.; Running, S.W. Development of a global evapotranspiration algorithm based on MODIS and global meteorology data. *Remote Sens. Environ.* **2007**, *111*, 519–536. [CrossRef]
21. Franks, S.W.; Beven, K.J.; Quinn, P.F.; Wright, I.R. On the sensitivity of soil-vegetation-atmosphere transfer (SVAT) schemes: Equifinality and the problem of robust calibration. *Agric. For. Meteorol.* **1997**, *86*, 63–75. [CrossRef]
22. Dickinson, R.E.; Henderson-Sellers, A.; Kennedy, P.J.; Wilson, M.F. *Biosphere-Atmosphere Transfer Scheme (Bats) for the NCAR Community Climate Model (No. NCAR/TN-275-+STR)*; University Corporation for Atmospheric Research: Boulder, CO, USA, 1986. [CrossRef]
23. Sellers, P.J.; Mintz, Y.; Sud, Y.C.; Dalcher, A. A simple biosphere model (SiB) for use within general circulation models. *J. Atmos. Sci.* **1986**, *43*, 505–531. [CrossRef]
24. Sellers, P.J.; Randall, D.A.; Collatz, G.J.; Berry, J.A.; Field, C.B.; Dazlich, D.A.; Zhang, C.; Collelo, G.D.; Bounoua, L. A revised land surface parameterization (SiB2) for atmospheric GCMs. Part I: Model Formulation. *J. Clim.* **1996**, *9*, 676–705. [CrossRef]
25. Liang, X.; Lettenmaier, D.P.; Wood, E.F.; Burges, S.J. A simple hydrologically based model of land surface water and energy fluxes for general circulation models. *J. Geophys. Res. Atmos.* **1994**, *99*, 14415–14428. [CrossRef]
26. Dai, Y.; Yuan, H.; Wei, N. The Common Land Model (Version 2014): User's Guide and Source Codes. 2014. Available online: http://globalchange.bnu.edu.cn/research/models (accessed on 20 April 2020).
27. Gao, Z.; Chae, N.; Kim, J.; Hong, J.; Choi, T.; Lee, H. Modeling of surface energy partitioning, surface temperature, and soil wetness in the Tibetan prairie using the Simple Biosphere Model 2 (SiB2). *J. Geophys. Res.* **2004**, *109*, D06102. [CrossRef]
28. Bounoua, L.; Masek, J.; Tourre, Y.M. Sensitivity of surface climate to land surface parameters: A case study using the simple biosphere model SiB2. *J. Geophys. Res.-Atmos.* **2006**, *111*, D22D09. [CrossRef]
29. Pongratz, J.; Bounoua, L.; DeFries, R.S.; Morton, D.C.; Anderson, L.O.; Mauser, W.; Klink, C.A. The impact of land cover change on surface energy and water balance in Mato Grosso, Brazil. *Earth Interact.* **2006**, *10*, 1–17. [CrossRef]
30. Yun, J.I.; Nam, J.C.; Hong, S.Y.; Kim, J.; Kim, K.S.; Chung, U.; Chae, N.Y.; Choi, T.J. Using Spatial Data and Land Surface Modeling to Monitor Evapotranspiration across Geographic Areas in South Korea. *Korean J. Agric. For. Meteorol.* **2005**, *6*, 149–163.
31. Xie, Z.; Yang, H.; Lv, H.; Lei, H.; Yang, D. Long-term observed evapotranspiration and its variation caused by anthropogenic controls in an ecofragile region. *Agric. Ecosyst. Environ.* **2022**, *335*, 108008. [CrossRef]
32. Zhang, L.; Jiang, H.; Wei, X.; Zhu, Q.; Liu, S.; Sun, P.; Liu, J. Evapotranspiration in the meso-scale forested watersheds in minjiang valley, west china. *J. Am. Water Resour. Assoc.* **2008**, *44*, 1154–1163. [CrossRef]
33. Thornthwaite, C.W. An Approach Toward a Rational Classification of Climate. *Geogr. Rev.* **1948**, *38*, 55–94. [CrossRef]
34. Zhou, J.; Yin, D.; Fan, Y.; Liu, T. Simulation and Analysis of Actual Evapotranspiration in Minjiang River Basin Based on Budyko Hypothesis. *J. Irrig. Drain.* **2017**, *36*, 107–112. [CrossRef]
35. Yin, D.; Fan, Y.; Zhou, J.; Liu, T. Simulation and Analysis of Actual Evapotranspiration in the Upper Reaches of Minjiang River Based on Fu Baopu Model. *China Rural Water Hydropower* **2016**, *2*, 33–36.
36. Fan, Y.; Yin, D.; Zhou, J.; Liu, T. Evapotranspiration Model Based on Complementary Relationship Theory in the Upper Reaches of Minjiang. *J. Irrig. Drain.* **2015**, *34*, 122–125. [CrossRef]
37. Luo, J. Analysis of annual runoff cycle of rivers: An example of major rivers in the upper Yangtze River. *Resour. Dev. Mark.* **1989**, *4*, 8–11.
38. Yang, K.; He, J. *China Meteorological Forcing Dataset (1979–2015)*; CSTR: 18406.11.westdc.002.2014.db; National Tibetan Plateau Data Center: Beijing, China, 2016. [CrossRef]
39. Resource and Environmental Science and Data Center, Chinese Academy of Sciences. Available online: https://www.resdc.cn/data.aspx?DATAID=284 (accessed on 20 April 2020).
40. Lu, L.; Liu, C. Chinese Soil Data Set Based on World Soil Database (hwsd) (v1.1). National Cryosphere Desert Data Center. Available online: http://www.ncdc.ac.cn (accessed on 20 April 2020).
41. Cui, X.; Liu, S.; Wei, X. Impacts of forest changes on hydrology: A case study of large watersheds in the upper reaches of Minjiang River watershed in China. *Hydrol. Earth Syst. Sci.* **2012**, *16*, 4279–4290. [CrossRef]
42. Zhang, L.; Sun, P.; Liu, S. Growing-season transpiration of typical forests in different succession stages in subalpine region of Western Sichuan, China. *Linye Kexue/Sci. Silvae Sin.* **2020**, *56*, 1–9. [CrossRef]
43. Sun, P.; Liu, S.; Jiang, H.; Lü, Y.; Liu, J.; Lin, Y.; Liu, X. Hydrologic effects of NDVI time series in a context of climatic variability in an Upstream Catchment of the Minjiang River. *J. Am. Water Resour. Assoc.* **2008**, *44*, 1132–1143. [CrossRef]